Supplement of Geosci. Model Dev., 18, 6963–6985, 2025
https://doi.org/10.5194/gmd-18-6963-2025-supplement

Geoscientific Model Development
Open Access

Supplement of

Aging and stress explain the earlier start of leaf senescence in trees in warmer years: translating the latest findings on senescence regulation into the DP3 model (v1.1)

Michael Meier et al.

Correspondence to: Michael Meier (michael.meier.1@unil.ch)

S1 Data

S1.1 Phenological data

S1.1.1 Coordinate transformation

The coordinates of the Swiss sites (Swiss phenology network, 2025) were transformed from the Swiss LV03 North and East projections (x and y [m]) to WGS84 latitude and longitude (φ and λ [°], respectively; Eqs. S1–S6; Sect. 2 in Geodesy, 2016):

$$x' = (x - 200000\,\mathrm{m})/1000000 \tag{S1}$$

$$y' = (y - 600000\,\mathrm{m})/1000000 \tag{S2}$$

$$\phi' = 2.6779094 + 4.728982\,y' + 0.791484\,y'x' + 0.1306\,y'x'^2 - 0.0436\,y'^3 \tag{S3}$$

$$\lambda' = 16.9023892 + 3.238272\,x' - 0.270978\,y'^2 - 0.002528\,x'^2 - 0.0447\,y'^2x' - 0.0140\,x'^3 \tag{S4}$$

$$\phi = \phi'/0.36 \tag{S5}$$

$$\lambda = \lambda'/0.36 \tag{S6}$$

S1.1.2 Relationship with latitude, longitude, and elevation

We related the average leaf senescence date per site to latitude, longitude, and elevation through linear regression models fitted separately for the average day of year when 50% and 100% of the leaves having turned color or having fallen (average LS50 and average LS100, respectively; Eq. S7; using the function lm in the R package stats; R Core Team, 2025):

$$\mathbf{y} = \mathbf{X}\boldsymbol{\beta} + \boldsymbol{\epsilon} \tag{S7}$$

$\mathbf{y}$ is the n_j-dimensional vector of the response variables average LS_{50} and average LS_{100}, where j refers to either response variable and n_j is the corresponding number of observations. $\mathbf{X}$ is the n_j×4 matrix with the values of the first column being set to 1 (for the intercept) and the 2nd to 4th columns containing the respective explanatory variables latitude [°], longitude [°], and elevation [m a.s.l.]. $\boldsymbol{\epsilon}$ is the n_j-dimensional vector of normally distributed errors with $N(0, \sigma_j^2)$. Thus, $\boldsymbol{\beta}$ is the 4-dimensional vector of the coefficient estimates for the intercept, latitude, longitude, and elevation.

The linear regression models revealed earlier average leaf senescence dates (i.e., aLS_{50} and aLS_{100}) with increasing latitude, increasing longitude, and increasing elevation (Table S1). Inline with recent research, this translates into earlier leaf senescence with cooler and more continental climatic conditions as well as with longer days during summer and faster decrease in day length between summer solstice and winter solstice (e.g., Kloos et al., 2024; Wang et al., 2022; but see Lu and Keenan, 2022).

Table S1. Coefficient estimates of the linear regression models

Response	Explanatory	Estimate	Standard error	*t* statistic	*p*-value	Adjusted R^2
average LS_{50} [doy]	Intercept	386.35	21.13	18.2837	0.000000	0.4761
	Latitude [°]	–1.69	0.40	-4.2079	0.000036	
	Longitude [°]	–1.61	0.15	-10.9693	0.000000	
	Elevation [m a.s.l.]	–0.0142	0.0031	-4.5542	0.000008	
average LS_{100} [doy]	Intercept	374.87	36.49	10.2731	0.000000	0.7614
	Latitude [°]	–0.95	0.70	-1.3631	0.175860	
	Longitude [°]	–1.62	0.27	-5.9722	0.000000	
	Elevation [m a.s.l.]	–0.0219	0.0049	-4.4497	0.000022	

Note: The linear regression models were fitted separately to the response variables average LS_{50} and average LS_{100} (i.e., the day of year [doy] when respective 50% and 100% of the leaves having turned color or having fallen). The coefficient estimates of the explanatory variables are given together with the corresponding standard errors, *t* statistic, and *p*-values. The adjusted R^2 is given for each model.

S1.2 Driver calculations

S1.2.1 Day length

Day length (L_{doy}) for a given day of year (*doy* [d]) was calculated from latitude (φ; [°]) according to Eqs. 1, 3, and 4 in Brock (1981; Eqs. S8–S10):

$$L_{doy} = 2\frac{W_{doy}}{15°\,\mathrm{h}^{-1}} \quad \text{(S8)}$$

$$W_{doy} = \arccos(-\tan(\varphi) * \tan(\gamma_{doy})) \quad \text{(S9)}$$

$$\gamma_{doy} = 23.45°\sin(360°(doy-81)/365) \quad \text{(S10)}$$

With γ_{doy} and W_{doy} being the respective declination [°] and hour-angle [°] at sunrise at *doy.*

S1.2.2 Photosynthetic activity

Sink limited daily net photosynthetic activity (Anet [mol C d^{-1}]; Eq. S11; Collatz et al., 1991) was calculated as the difference between the gross photosynthetic activity (A_{grs} [mol C d^{-1}]) and respiration (R [mol C d^{-1}]; Collatz et al., 1991; Farquhar et al., 1980; Wohlfahrt and Gu, 2015).

$$A_{net} = A_{grs} - R \quad \text{(S11)}$$

A_{grs} in turn depended on photon availability (J_E [mol C d^{-1}]), Rubisco activity (J_C [mol C d^{-1}]), and sink capacity (J_S [mol C d^{-1}]; Eq. S12), while R was defined as a fraction of the maximum photosynthetic rate (V_{max} [mol C d^{-1}]; Eq. S13).

$$A_{grs} = \max\left(0,\quad L \times \frac{J_P + J_S - \sqrt{(J_P + J_S)^2 - 4\beta_C J_P J_S}}{2\beta_C}\right) \quad \text{(S12)}$$

$$R=b_{C3}V_{max} \tag{S13}$$

J_P is an intermediate variable, combining J_E and J_C (Eq. S14), β_C is a constant shape parameter, and b_{C3} is a constant fraction for C3 plants (Table S1).

$$J_P=\frac{J_C+J_E-\sqrt{(J_C+J_E)^2-4\theta_C J_E J_C}}{2\theta_C} \tag{S14}$$

θ_C is a constant shape parameter (Table S1). J_E and J_C are daily fractions of the available photosynthetically active radiation ($APAR$ [W m^{-2}]; Eq. S15) and V_{max} (Eq. S16), respectively, while J_S is a constant fraction of V_{max} (Eq. S17).

$$J_E=C_1\times {APAR}/{L} \tag{S15}$$

$$J_C=C_2\times {V_{max}}/{24[\mathrm{h}]} \tag{S16}$$

$$J_S=0.5\times {V_{max}}/{24[\mathrm{h}]} \tag{S17}$$

L is the day length [h], and V_{max} depends on $APAR$ (Eq. S18), which in turn was calculated as a fraction (*fa-par*) of the photosynthetically active radiation (PAR [W m^{-2}]; Eq. S19).

$$V_{max}={1}/{b_{C3}}\ {C_1}/{C_2}\,[(2\theta-1)s-\sigma(2\theta s-C_2)]\,APAR \tag{S18}$$

$$APAR=\alpha_a c_q\, fapar\, PAR(3600\times 24)[\mathrm{s}] \tag{S19}$$

θ is a constant shape parameter, while α_a and c_q are a constant ratio and a constant conversion factor for the respective assimilation and conversion of solar radiation (Table S1). While *fapar* depended on the leaf area index (*LAI*; Eq. S20), *PAR* was derived from the surface shortwave down welling radiation (R_s [W m^{-2}]; Eq. S21).

$$fapar=1e^{-0.5\,LAI} \tag{S20}$$

$$PAR=0.5\,R_s \tag{S21}$$

V_{max} further depends on s and σ (Eqs. S22–S23) as well as on C_1 and C_2 (Eqs. S24–S25).

$$s=b_{C3}\ {24[\mathrm{h}]}/{L} \tag{S22}$$

$$\sigma=\sqrt{1-\frac{C_2-s}{C_2-\theta s}} \quad \text{(S23)}$$

$$C_1=\phi_C \alpha_{C3} f(T)\times\frac{p_{i,CO2}-\Gamma_*}{p_{i,CO2}+2\Gamma^*} \quad \text{(S24)}$$

$$C_2=\frac{(p_{i,CO2}-\Gamma_*)}{p_{i,CO2}+K_C(1+{p_{a,O2}}/{K_O})} \quad \text{(S25)}$$

α_{C3} describes the quantum efficiency of C3 plants, and $p_{a,O2}$ is the ambient partial O_2 pressure (Table S1). $p_{i,CO2}$ is the internal partial CO_2 pressure (Eq. S26), Γ_* is the CO_2 condensation point (Eq. S27), K_C and K_O are the kinetic coefficients for CO_2 (Eq. S28) and O_2 (Eq. S29), respectively, and *f(T)* is a function of the mean temperature (Eq. S30).

$$p_{i,CO2}=\lambda_{C3}[CO_2]_A 10^{-16} p_0 \quad \text{(S26)}$$

$$\Gamma_*=\frac{p_{a,O2}}{2\tau q_{\tau 10}^{(T-25K)/10}} \quad \text{(S27)}$$

$$K_C=k_C q_{C10}^{(T-25\mathrm{K})/10} \quad \text{(S28)}$$

$$K_O=k_O q_{O10}^{(T-25\mathrm{K})/10} \quad \text{(S29)}$$

$$f(x)=\min\left(1,\quad \max\left(0,\quad \frac{1}{1+e^{k_1(k_2-T)}}\times\left(1-0.01e^{k_3(T-x_3)}\right)\right)\right) \quad \text{(S30)}$$

λ_{C3} is the optimal ratio of internal to ambient CO_2 pressure of C3 plants. τ, k_C, and k_O are the specificity ratio CO_2:O_2 and the Michaelis constants for CO_2 and O_2, respectively, while $q_{\tau 10}$, q_{C10}, and q_{O10} are the corresponding rates of change due to a 10 K change in mean temperature (T [°C]). k_1, k_2, and k_3 are derived from the cardinal temperatures x_1, x_2, x_3, and x_4 (Eqs. S31–S33, Table S1).

$$k_1=\frac{2\log(1/0.99-1)}{x_1-x_2} \quad \text{(S31)}$$

$$k_2=(x_1+x_2)/2 \quad \text{(S32)}$$

$$k_3=\log\left(\frac{0.99/0.01}{x_4-x_3}\right) \quad \text{(S33)}$$

Table S2. Constants.

Constant	Value	Description	Source
β_C	0.95	Fraction; Co-limitation (shape) parameter for J_P and J_S	Co97, Eq. (A9)
b_{C3}	0.015	Fraction; Leaf respiration per maximum Rubisco capacity for C3 plants	HP96, Table 2
θ_C	0.98	Fraction; Co-limitation (shape) parameter for J_C and J_E	Co97, Eq. (A8)
θ	0.7	Fraction; Alternative co-limitation (shape) parameter for J_C and J_E	Table 2 in HP96
α_a	0.5	Ratio; Assimilated PAR from ecosystem to leaf level	Table 4 in Si00
c_q	4.6×10^{-6}	[E J^{-1}], [mol J^{-1}]; Conversion factor for solar radiation at 550 nm	
α_{C3}	0.08	Intrinsic quantum efficiency of CO_2 uptake in C3 plants	Ha96; Si00
p_0	1.013×10^5	[Pa]; Standard pressure	-
$P_{a,O2}$	$0.209 \times p_0$	[Pa]; Ambient O_2 pressure	Table A1 in Co97; Table 2 in HP96
λ_{C3}	0.8	Fraction	Ge04
τ	2600	Ratio; CO_2:O_2 specificity ratio	Table A1 in Ca91
k_O	3×10^4	[Pa]; Michaelis constant for O_2	Table A1 in Co97; Table 2 in HP96
k_C	30	[Pa]; Michaelis constant for CO_2	
$q_{\tau 10}$	0.57	Fraction; Temperature-sensitivity of τ regarding a change of 10 K	Table A1 in Ca91
q_{O10}	1.2	Fraction; Temperature-sensitivity of k_O regarding a change of 10 K	Table A1 in Co97; Table 2 in HP96
q_{C10}	1.2	Fraction; Temperature-sensitivity of k_C regarding a change of 10 K	
x_1	1	[°C]; Cardinal temperatures	Eqs. S10–S15 in Za20
x_2	18		
x_3	25		
x_4	45		

Note: These constants were taken from the following sources: Co91: (Collatz et al., 1991); Ge04: (Gerten et al., 2004); Ha96: (Haxeltine et al., 1996); HP96: (Haxeltine and Prentice, 1996); Si00: (Sitch et al., 2000); Za20: (Zani et al., 2020).

S1.2.3 Keetch and Byram drought index

The Keetch and Byram drought index for day *i* (Q_i; Eq. S34) was calculated from daily precipitation (P_i) and daily maximum temperature (Tx_i; Keetch and Byram, 1968), which were converted from millimeters [mm] to inches [in] and from degree Celsius [°C] to degree Fahrenheit [°F], respectively (P'_i and Tx'_i; Eqs. S35–S36; Foster et al., 1981, Table 2; Shaw, 1931; Woods, 1931):

$$Q_i = \min\left(800,\quad \max\left(0,\quad Q_{Base,i} + \Delta Q_i\right)\right) \tag{S34}$$

$$P'_i = {P_i}/{25.4[\text{mm in}^{-1}]} \tag{S35}$$

$$Tx'_i = 9/5[°\text{F } °\text{C}^{-1}] \times Tx_i + 32[°\text{F}] \tag{S36}$$

The base index ($Q_{base,i}$) was derived from Q of the previous day (i.e., Q_{i-1}) and the net precipitation of the given day ($P_{net,i}$ [in]; Eq. S37), while the daily drought factor (ΔQ_i) was calculated from the base index ($Q_{base,i}$), Tx'_i, and mean annual rainfall (R_i, [in]; Eqs. S38–S39):

$$Q_{Base,i} = \max(0,\quad Q_{i-1} - 100\,P_{net,i}) \tag{S37}$$

$$\Delta Q_i = (800 - Q_{Base,i}) \times \frac{0.968\,e^{0.0486\,Tx'_i} - 0.83}{1 + 10.88\,e^{-0.0441\,R_i}} \times 0.001 \tag{S38}$$

$$R_i = \frac{1}{366} \sum_{j=i-355}^{i} P'_j \tag{S39}$$

Here, $Q_{Base,1}$ (i.e., of January 1st, 1950) was set to the average Q_{Base} during the Decembers and Januaries of 1955–1959, $R_1, R_2, \ldots, R_{355} = R_{366}$, and $P'_i = 0$ if the precipitation fell as snow (i.e., if the mean temperature $T_i \leq 0$ °C). P_{net} depends on P' of the given and two previous days in comparison to a threshold precipitation of 0.2 in (Y_P; Eq. S40).

$$P_{net,i} = \begin{cases} \max(0,\quad P'_i - Y_P) & , \quad if \quad P'_{i-1} = 0 \\ P'_i & , \quad if \quad P'_{i-1} \geq Y_P \\ \max\left(0,\quad \sum_{k=0}^{1} P'_{i-k} - Y_P\right) & , \quad if \quad P'_{i-1} < Y_P \;\wedge\; \sum_{k=1}^{2} P'_{i-k} \geq Y_P \\ \max\left(0,\quad \sum_{k=0}^{2} P'_{i-k} - Y_P\right) & , \quad if \quad P'_{i-1} < Y_P \;\wedge\; \sum_{k=1}^{2} P'_{i-k} < Y_P \end{cases} \tag{S40}$$

The KBDI was initiated per site, i.e., setting Q_i to zero after the first period of either abundant precipitation or snow melt during 1950–1954 (Keetch and Byram, 1968). A period of abundant precipitation was defined as seven consecutive days during which the precipitation sum was six inches (i.e., 152.4 mm; see Eq. S34) or more. A period of snow melt was defined as four consecutive days during which the snow melt followed on at least seven days with snow fall. For this, we defined day i as a day with snow melt when $T_i > 0$ °C and as a day with snow fall when $P_i > 0$ mm and $T_i \leq 0$ °C.

S2 Methods

S2.1 Initial ranges for parameters

Table S3. Ranges for parameter calibration

Symbol	Meaning	Boundaries
$-a_C$	Boundary below which cold stress is 1 versus 0	0–30 °C
$b_{0,C}$	Boundary above which cold stress gradually increases from 0 to 1	0–30 °C
$b_{1,C}$	Boundary below which cold stress gradually decreases from 1 to 1	($b_{0,C}$+0 °C)–($b_{0,C}$+20 °C)
$-a_P$	Boundary below which photoperiod stress is 1 versus 0	–0.25–+0.25 h
$b_{0,P}$	Boundary above which photoperiod stress gradually increases from 0 to 1	–0.25–+0.25 h
$b_{1,P}$	Boundary below which photoperiod stress gradually decreases from 1 to 0	($b_{0,P}$+0 h)–($b_{0,P}$+0.3 h)
a_D	Boundary above which dry stress is 1 versus 0	0–800
$-b_{0,D}$	Boundary above which dry stress gradually increases from 0 to 1	0–800
$-b_{1,D}$	Boundary below which dry stress gradually decreases from 1 to 0	($b_{0,D}$+0)–($b_{0,D}$+400)
a_R	Boundary above which rain stress is 1 versus 0	0–500 mm
$-b_{0,R}$	Boundary above which rain stress gradually increases from 0 to 1	0–500 mm
$-b_{1,R}$	Boundary below which rain stress gradually decreases from 1 to 0	($b_{0,R}$+0 mm)–($b_{0,R}$+300 mm)
a_H	Boundary above which heat stress is 1 versus 0	25–50 °C
a_N	Boundary above which nutrient stress is 1 versus 0	20–250 mol C d^{-1}
$-a_F$	Boundary below which frost stress is 1 versus 0	–5–+10 °C
w_C	Weight of cold stress	0–1
w_P	Weight of photoperiod stress	0–1
w_D	Weight of dry stress	0–1
w_R	Weight of rain stress	0–1
w_H	Weight of heat stress	0–1
w_N	Weight of nutrient stress	0–1
w_F	Weight of frost stress	0–1
w_A	Weight of aging rate	0–1
w_S	Weight of stress rate	0–1
s_X	Scaling factor of the senescence rate	0–1
x_S	Shape parameter of the stress rate	0–10
c	First parameter of exponential function	0.005–0.5
d	Second parameter of exponential function	0–15
$Y_{Aging,1}$	Threshold for the aging state, marking the transition from young to mature leaf	0–50 d
$Y_{Aging,2}$	Threshold for the aging state, marking the transition from mature to old leaf	$Y_{Aging,1}$–($Y_{Aging,1}$+250 d)
Y_{LS100}	Threshold for the senescence state, indicating the day of LS_{100}	0–10

Note: The symbols of the parameters for the boundaries below or above which stress occurs [a; see response function $g(x)$; Eq. 7], for the boundaries between which stress occurs [b_0 and b_1; see response function $h(x)$; Eq. 8], and for the weights (w) that define the stress rate as well as for the different formulations of the senescence rate (w_A, w_S, s_X, x_S, c, and d; Eq. 9) and the thresholds (Y) that mark the transitions from young to mature leaf, the transition from mature to old leaf and the time when 100% of the leaves having changed color or having fallen (LS_{100}).

S2.2 Controls of the simulated annealing algorithm

The choice of the controls for the optimization algorithm influences the accuracy of the calibrated model (Meier and Bigler, 2023) through the exploration–exploitation trade-off (Candelieri, 2021; Maes et al., 2013). Thus, we set the controls 'maximum iterations', 'maximum calls', and 'temperature' of the generalized simulated annealing algorithm (Xiang et al., 1997, 2017) in such a way that the calibrated model resulted in most accurate predictions for the validation sample. To identify these optimal controls for each model and calibration sample, we calibrated each model four times (i.e., twice with each sample draw) with all 27 combinations of 4000, 5000, and 6000 maximum iterations, 10^6, 10^7, and

10^8 maximum calls, as well as temperatures of 5200, 5230, and 5300. Thus, we used the combination of controls that resulted in the lowest average Akaike information criterion for small samples (i.e., $n < 40k$; AICc; Eq. S41; based on the validation sample; Akaike, 1974; Burnham and Anderson, 2004) to compute the additional six calibration runs (i.e., three per calibration sample; Table S4).

$$AICc = AIC + \frac{2k(k+1)}{n-k-1} \quad \text{(S41)}$$

$$AIC = -2 \times \log(L) + 2k \quad \text{(S42)}$$

$$\sigma_e = \sqrt{\frac{1}{n}\sum_{i=1}^{n}(x_{p,i} - x_{o,i})^2} \quad \text{(S43)}$$

n is the number of predicted and observed doy pairs (x_p and x_o, respectively) and k is the number of free model parameters. L is the likelihood for the normally distributed model errors (i.e., $x_p - x_o$; Fisher and Russell, 1997) with $N(0, \sigma_e)$. In case $S_{Senescence}$ did not reach the thresholds $Y_{LS_{50}}$ and $Y_{LS_{100}}$ until December 31st, corresponding x_p were considered missing and thus set to doy 367 before their accuracy was evaluated.

Table S4. Optimal controls of the generalized simulated annealing algorithm.

Model	Sample	Maximum iterations	Maximum calls	Temperature
CDD	LS_{50}	4000	10^8	5300
DM2	LS_{50}	6000	10^6	5300
PIA	LS_{50}	5000	10^7	5200
DP3	LS_{50}	4000	10^8	5300
	LS_{50}-LS_{100}	5000	10^7	5200

Note: Only the control settings for the evaluated models (LS_{50} sample) and for the model that was selected through the iterations of model development (LS_{50}-LS_{100} sample) are shown. Those for the models that were rejected during model development are omitted.

S2.3 Model calibration, selection, and evaluation

All models were calibrated by minimizing the root mean squared error (RMSE; Eq. S44).

$$RMSE = \sqrt{\frac{1}{n}\sum_{i=1}^{n}(x_{p,i} - x_{o,i})^2} \quad \text{(S44)}$$

Thus, for each model, we selected and further evaluated the calibration run that resulted in highest modified Kling-Gupta efficiency (KGE'; Eq. S45; Gupta et al., 2009; Kling et al., 2012) for the validation sample.

$$KGE' = 1 - \sqrt{(\rho-1)^2 + (\beta-1)^2 - (\gamma-1)^2} \quad \text{(S45)}$$

$$\beta = {}^{\mu_p}\!/_{\mu_o} \tag{S46}$$

$$\gamma = \frac{\sigma_p / \mu_p}{\sigma_o / \mu_o} \tag{S47}$$

β is the bias ratio, γ is the variability ratio, and ρ is the Pearson correlation between x_p and x_o. μ_p and μ_o, are the respective predicted and observed mean doy, and σ_p and σ_o are the corresponding standard deviations. For the perfect model (i.e., $x_p = x_o$ for all i), $\rho = 1$, $\beta = 1$, and $\gamma = 1$, and thus $KGE' = 1$, whereas $1 > KGE' > -\infty$ for imperfect models.

S2.4 Linear mixed-effects model and analysis of variance

We fitted a linear mixed-effects model (LMM; Eq. S48; Pinheiro and Bates, 2000; Wood, 2011, 2017) to analyze the effects on the model error:

$$\mathbf{y} = \mathbf{X}\boldsymbol{\beta} + \mathbf{Z}\mathbf{b} + \boldsymbol{\epsilon} \tag{S48}$$

$\mathbf{y}$ is the n-dimensional vector of the response variable ‘model error’ (ME) and n is the corresponding number of ME. $\mathbf{X}$ is the $n \times p$ matrix of the intercept (i.e., 1) and the $p - 1$ explanatory variables. $\boldsymbol{\beta}$ is the corresponding p-dimensional vector of the fixed effects ‘country’ and ‘model’ as well as the annual and site-specific deviations in mean annual temperature, mean annual KBDI, accumulated A_{net} between LU and summer solstice, latitude, and elevation (CTR, MOD, δMAT, δMAQ, δA_{net}, δLAT and δELV, respectively) from the overall calibration sample means per variable. $\mathbf{Z}$ is the $n \times q$ matrix of the random effects, assigning the n observations to the q groups of the grouping variable ‘site’ (STE). $\mathbf{b}$ is the corresponding q-dimensional vector of the random intercepts with $\mathbf{b} \sim N(0, \sigma^2_{\mathbf{b}}\mathbf{I}_q)$, and $\boldsymbol{\epsilon}$ is the n-dimensional vector of the errors with $\boldsymbol{\epsilon} \sim N(0, \sigma^2\mathbf{I}_n)$ (Baayen et al., 2008; Chpt. 2.1 in Pinheiro and Bates, 2000; Chpt. 6.2 in Wood, 2017).

We fitted this LMM with the function bam in the R package mgcv (Wood, 2017), using the following formula (Eq. S49):

```
ME ~ MOD * (δMAT + δMAQ + δAnet + δLAT + δELV) + CTR + s(STE, bs = 're')          (S49)
```

This LMM combined model effects interacting with effects due to climatic deviations from the calibration sample (red), spatial deviations from the calibration sample (green), and data structure (blue). The LMM was the basis for the type-III ANOVA (Yates, 1934), which we derived with the functions aov and drop1 in the R package stats (Eq. S50; R Core Team, 2025):

```
drop1(aov(LMM), scope = ~., test = "F")          (S50)
```

Thus, we calculated the amount of variation attributed to differences among each explanatory variable, i.e., the relative impact of given variable on the variance in the model error explained by the LMM, by dividing the variable-specific sum of squares by the total sum of squares over all variables.

S3 Results

S3.1 Formulation of the leaf development process

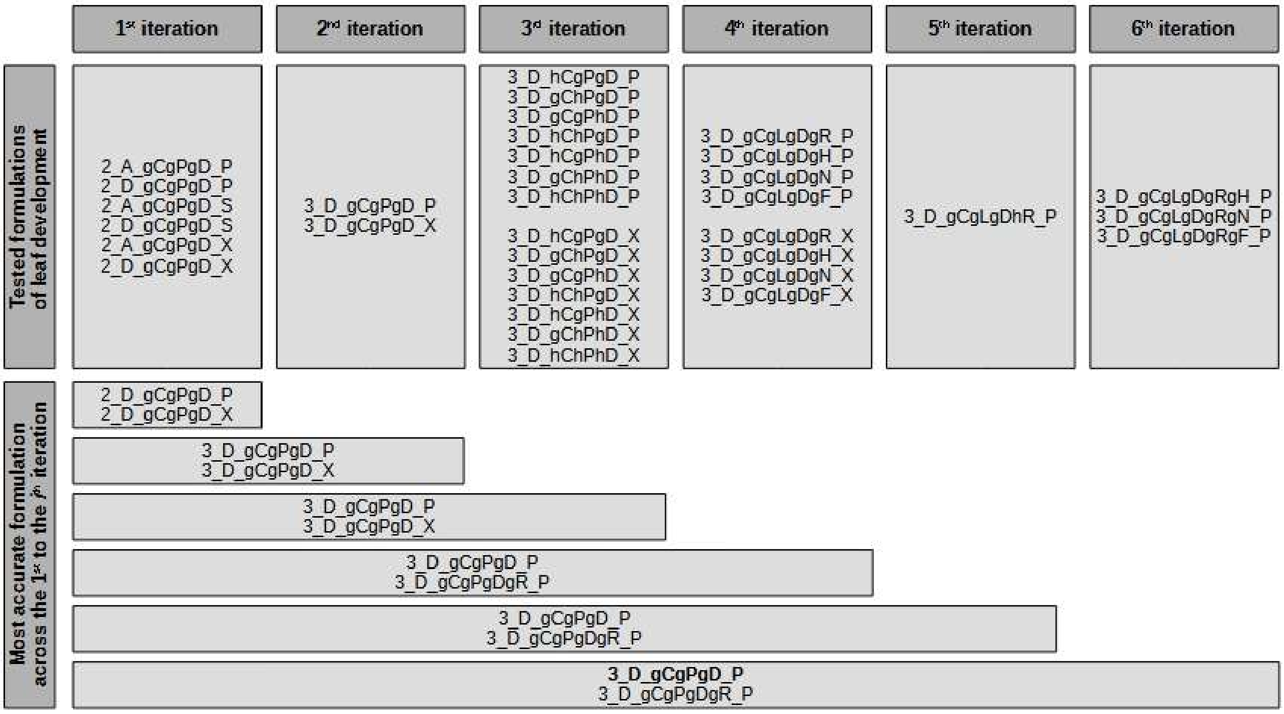

Figure S1. Tested models. The tested models were labeled according to their formulation, namely as $x_P\_x_A\_x_S\_x_X$, with x_P being the number of leaf development phases (i.e., 2 or 3), x_A being the driver of the aging rate (i.e., A or D for photosynthesis or days, respectively), x_S being the stress rate in response [i.e., g or h for *g(x)* or *h(x)*] to the stressors cold (C), shortening (P), dry (D), heat (H), and frost (F) days, heavy rain periods (R), and nutrient depletion (N), and x_X indicating the formulation of the senescence rate (i.e., S, P, or X when formulated as a sum, product, or exponential function of aging and stress, respectively). After each iteration, we identified the two most accurate models across the given and all previous iterations (Fig, 5, Sect. 2.5). These models were further developed through the next iteration. As soon as such a subsequent iteration did not produce any new model, we selected the most accurately formulated model among all iterations (bold; i.e., the 'DP3' model). All models were tested for beech based on the LS_{50}-LS_{100} sample (Sect. 2.4).

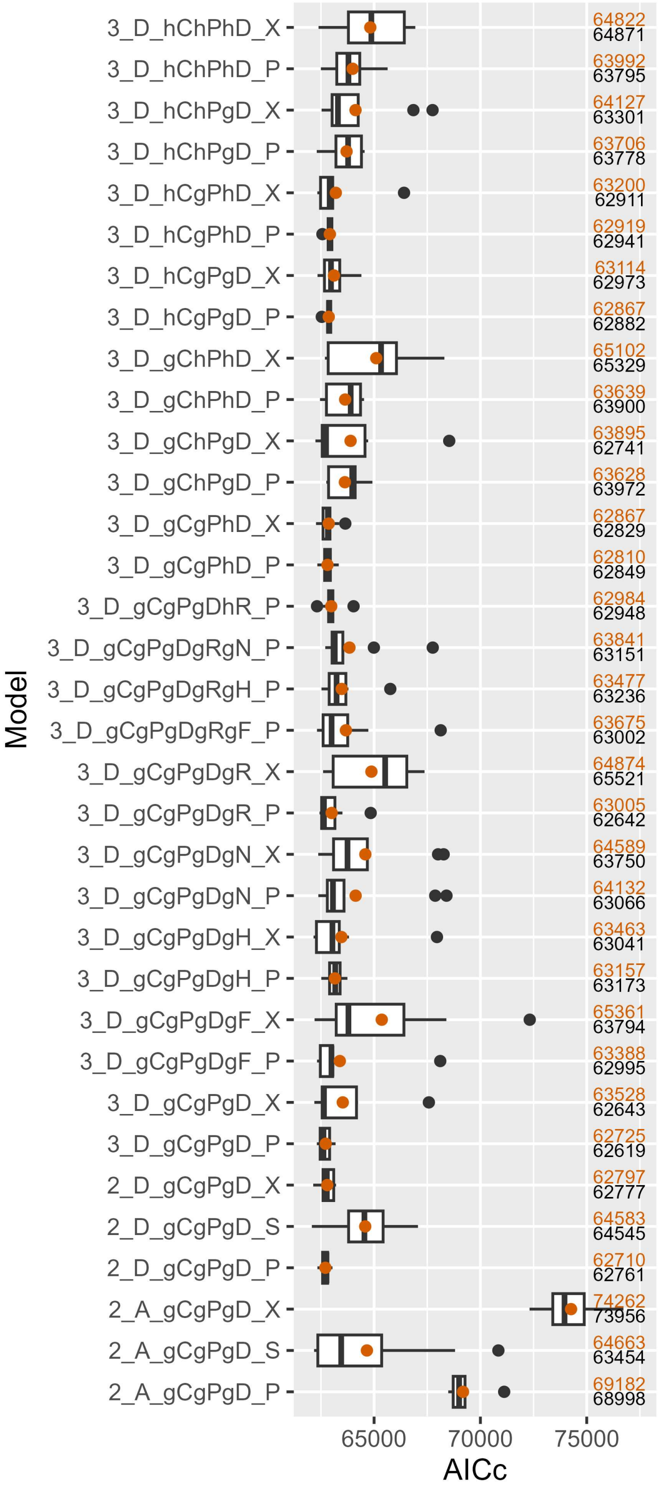

Figure S2. Accuracy of the tested model formulations. The accuracy was assessed with the Akaike information criterion for small samples (AICc; Eq. S40). The boxes indicate the inner quartile range and the median (middle line). The most extreme values are indicated with dots if outside ±1.5 times the inner quartile range from the 1st and 3rd quartile, and with whiskers otherwise. Orange dots show the mean, which is further indicated in orange to the right of each box, together with the median indicated in black. The models were labeled as $x_P\_x_A\_x_S\_x_X$, with x_P being the number of leaf development phases (i.e., 2 or 3), x_A being the driver of the aging rate (i.e., A or D for photosynthesis or days, respectively), x_S being the stress rate that is the summed response [i.e., g or h for *g(x)* or *h(x)*] to the stressors cold (C), shortening (P), dry (D), heat (H), and frost days (F), heavy rain periods (R), and nutrient depletion (N), and x_X indicating the formulation of the senescence rate (i.e., S, P, or X when formulated as a sum, product, or exponential function of aging and stress, respectively). All models were calibrated with the LS_{50}-LS_{100} sample (Sect. 2.4).

Table S5. Senescence summarized across mean annual temperature

Calibration	Subject	Variable	3.8–6.1 °C	6.1–8.4 °C	8.4–10.7 °C	10.7–13.0 °C	13.0–15.4 °C
LS_{50}-LS_{100}	Size	Site-years	329	2325	3652	570	48
	Timing	SI [doy]	172.90	164.42	156.36	151.31	149.42
		LS_{50} [doy]	291.86	291.20	288.15	282.21	270.65
		LS_{100} [doy]	290.30	290.05	291.77	296.65	-
	Duration	LS_{50}–SI [d]	118.96	126.80	131.79	130.92	121.23
		LS_{100}–SI [d]	123.90	123.94	134.81	144.23	-
	Cause	Stress	0.77	0.66	0.61	0.66	0.94
		Aging	0.21	0.33	0.38	0.33	0.04
		Both	0.02	0.01	0.01	0.01	0.02
	Stressors SI	Cold	0.46	0.52	0.41	0.28	0.15
		Photoperiod	0.54	0.48	0.58	0.71	0.85
		Dry	0.00	0.00	0.01	0.01	0.00
	Stressors LS_{50}	Cold	0.56	0.64	0.57	0.41	0.12
		Photoperiod	0.44	0.36	0.42	0.59	0.88
		Dry	0.00	0.00	0.00	0.01	0.00
	Stressors LS_{100}	Cold	0.06	0.11	0.15	0.20	-
		Photoperiod	0.94	0.89	0.85	0.80	-
		Dry	0.00	0.00	0.00	0.00	-
LS_{50}	Size	Site-years	334	2346	3620	542	45
	Timing	SI [doy]	132.15	124.48	116.44	111.36	109.51
		LS_{50} [doy]	282.96	283.43	283.36	282.98	282.84
	Duration	LS_{50}–SI [d]	150.81	158.95	166.92	171.62	173.33
	Cause	Stress	0.99	1.00	0.96	0.91	0.93
		Aging	0.01	0.00	0.03	0.07	0.07
		Both	0.01	0.00	0.01	0.02	0.00
	Stressors SI	Cold	0.09	0.15	0.26	0.40	0.38
		Photoperiod	0.91	0.85	0.74	0.60	0.62
		Dry	0.00	0.00	0.00	0.00	0.00
	Stressors LS_{50}	Cold	0.00	0.00	0.00	0.01	0.01
		Photoperiod	1.00	1.00	1.00	0.99	0.99
		Dry	0.00	0.00	0.00	0.00	0.00

Note: The summary is structured in the subjects bin size (‘size’), timing, duration, cause, and stressors. Size is given by the count of the evaluated variable site-years. Timing is indicated by the mean day of year [doy] of senescence induction (SI) and of the stages when 50% and 100% of the leaves having turned color or having fallen (LS_{50} and LS_{100}, respectively). Duration refers to the periods from SI to LS_{50} and to LS_{100} (LS_{50}–SI and LS_{100}–SI, respectively) and is given in days [d]. Cause is assessed by the relative number of site-years during which aging versus stress induced senescence (i.e., reached their thresholds first), while the variable both refers to aging and stress reaching their thresholds on the same day. Stressors (i.e., cold stress, photoperiod stress, and dry stress) are compared by their relative contribution to the stress rate that has accumulated by SI, LS_{50}, and LS_{100}. The underlying model was calibrated with the LS_{50}-LS_{100} and LS_{50} samples (Sect. 2.4).

Table S6. Senescence summarized across mean annual Keetch and Byram drought index

Calibration	Subject	Variable	2.7–23.5	23.5–44.2	44.2–65.0	65.0–85.7	85.7–107.0
LS_{50}-LS_{100}	Size	Site-years	6603	270	45	4	2
	Timing	SI [doy]	159.65	154.16	153.60	156.50	150.00
		LS_{50} [doy]	288.63	290.92	291.98	297.00	291.50
		LS_{100} [doy]	291.15	292.92	303.33	-	-
	Duration	LS_{50}–SI [d]	128.98	136.73	138.34	140.50	141.50
		LS_{100}–SI [d]	129.21	139.84	148.67	-	-
	Cause	Stress	0.65	0.50	0.36	0.50	0.50
		Aging	0.34	0.49	0.64	0.50	0.50
		Both	0.01	0.00	0.00	0.00	0.00
	Stressors SI	Cold	0.43	0.56	0.74	0.79	0.50
		Photoperiod	0.56	0.43	0.26	0.21	0.50
		Dry	0.01	0.00	0.00	0.00	0.00
	Stressors LS_{50}	Cold	0.57	0.71	0.77	0.92	1.00
		Photoperiod	0.43	0.29	0.23	0.08	0.00
		Dry	0.00	0.00	0.00	0.00	0.00
	Stressors LS_{100}	Cold	0.13	0.14	0.35	-	-
		Photoperiod	0.87	0.86	0.65	-	-
		Dry	0.00	0.00	0.00	-	-
LS_{50}	Size	Site-years	6578	263	39	5	2
	Timing	SI [doy]	119.76	113.81	113.77	116.00	110.00
		LS_{50} [doy]	283.32	283.64	283.08	285.00	284.50
	Duration	LS_{50}–SI [d]	163.56	169.83	169.31	169.00	174.50
	Cause	Stress	0.97	0.94	0.85	1.00	1.00
		Aging	0.02	0.04	0.13	0.00	0.00
		Both	0.01	0.02	0.03	0.00	0.00
	Stressors SI	Cold	0.22	0.32	0.22	0.04	0.61
		Photoperiod	0.78	0.68	0.78	0.96	0.39
		Dry	0.00	0.00	0.00	0.00	0.00
	Stressors LS_{50}	Cold	0.00	0.00	0.00	0.00	0.00
		Photoperiod	1.00	1.00	1.00	1.00	1.00
		Dry	0.00	0.00	0.00	0.00	0.00

Note: See Table S5.

Table S7. Senescence summarized across latitude

Calibration	**Subject**	**Variable**	**45.8–48.3 °N**	**48.3–50.7 °N**	**50.7–53.1 °N**	**53.1–55.6 °N**	**55.6–58 °N**
LS_{50}-LS_{100}	Size	Site-years	3709	1792	884	512	27
	Timing	SI [doy]	160.66	157.82	157.32	159.14	160.96
		LS_{50} [doy]	283.32	294.36	294.96	298.69	275.42
		LS_{100} [doy]	289.14	295.61	296.53	293.06	290.43
	Duration	LS_{50}–SI [d]	122.66	136.52	137.58	139.65	114.54
		LS_{100}–SI [d]	124.34	141.34	141.64	135.67	130.33
	Cause	Stress	0.79	0.48	0.48	0.42	0.96
		Aging	0.21	0.51	0.51	0.57	0.04
		Both	0.01	0.01	0.01	0.01	0.00
	Stressors SI	Cold	0.30	0.64	0.58	0.64	0.13
		Photoperiod	0.70	0.36	0.41	0.35	0.87
		Dry	0.01	0.00	0.01	0.00	0.00
	Stressors LS_{50}	Cold	0.41	0.78	0.72	0.89	0.19
		Photoperiod	0.59	0.21	0.28	0.11	0.81
		Dry	0.00	0.00	0.00	0.00	0.00
	Stressors LS_{100}	Cold	0.10	0.14	0.20	0.17	0.10
		Photoperiod	0.90	0.86	0.80	0.83	0.90
		Dry	0.00	0.00	0.00	0.00	0.00
LS_{50}	Size	Site-years	3722	1739	887	511	28
	Timing	SI [doy]	120.85	117.89	117.16	119.05	120.68
		LS_{50} [doy]	283.29	283.37	283.43	283.34	283.71
	Duration	LS_{50}–SI [d]	162.44	165.47	166.27	164.29	163.04
	Cause	Stress	0.98	0.96	0.96	0.97	1.00
		Aging	0.02	0.03	0.03	0.03	0.00
		Both	0.01	0.01	0.01	0.01	0.00
	Stressors SI	Cold	0.21	0.26	0.25	0.22	0.12
		Photoperiod	0.79	0.74	0.75	0.78	0.88
		Dry	0.00	0.00	0.00	0.00	0.00
	Stressors LS_{50}	Cold	0.00	0.00	0.00	0.00	0.00
		Photoperiod	1.00	1.00	1.00	1.00	1.00
		Dry	0.00	0.00	0.00	0.00	0.00

Note: See Table S5.

Table S8. Senescence summarized across elevation

Calibration	Subject	Variable	–1–288 m	288–576 m	576–864 m	864–1150 m	1150–1440 m
LS_{50}-LS_{100}	Size	Site-years	2023	2767	1329	666	139
	Timing	SI [doy]	156.43	157.27	162.20	168.12	176.01
		LS_{50} [doy]	293.58	287.55	282.78	287.59	305.68
		LS_{100} [doy]	293.29	289.58	290.45	289.03	-
	Duration	LS_{50}–SI [d]	137.14	130.28	120.62	119.47	129.67
		LS_{100}–SI [d]	137.61	131.46	123.19	123.08	-
	Cause	Stress	0.48	0.64	0.81	0.76	0.65
		Aging	0.50	0.35	0.19	0.23	0.33
		Both	0.01	0.01	0.01	0.01	0.01
	Stressors SI	Cold	0.55	0.41	0.32	0.41	0.77
		Photoperiod	0.44	0.59	0.67	0.58	0.23
		Dry	0.00	0.01	0.00	0.00	0.00
	Stressors LS_{50}	Cold	0.74	0.54	0.43	0.50	0.87
		Photoperiod	0.26	0.46	0.56	0.49	0.13
		Dry	0.00	0.00	0.00	0.00	0.00
	Stressors LS_{100}	Cold	0.16	0.13	0.12	0.06	-
		Photoperiod	0.84	0.87	0.88	0.94	-
		Dry	0.00	0.00	0.00	0.00	-
LS_{50}	Size	Site-years	2018	2687	1368	681	133
	Timing	SI [doy]	116.42	117.43	122.23	128.10	135.60
		LS_{50} [doy]	283.32	283.33	283.40	283.25	283.29
	Duration	LS_{50}–SI [d]	166.90	165.90	161.17	155.15	147.68
	Cause	Stress	0.95	0.97	0.98	1.00	1.00
		Aging	0.04	0.02	0.01	0.00	0.00
		Both	0.01	0.01	0.01	0.00	0.00
	Stressors SI	Cold	0.28	0.25	0.17	0.12	0.05
		Photoperiod	0.72	0.75	0.83	0.88	0.95
		Dry	0.00	0.00	0.00	0.00	0.00
	Stressors LS_{50}	Cold	0.00	0.00	0.00	0.00	0.00
		Photoperiod	1.00	1.00	1.00	1.00	1.00
		Dry	0.00	0.00	0.00	0.00	0.00

Note: The bins of elevation are given in m a.s.l.. For further notes see Table S5.

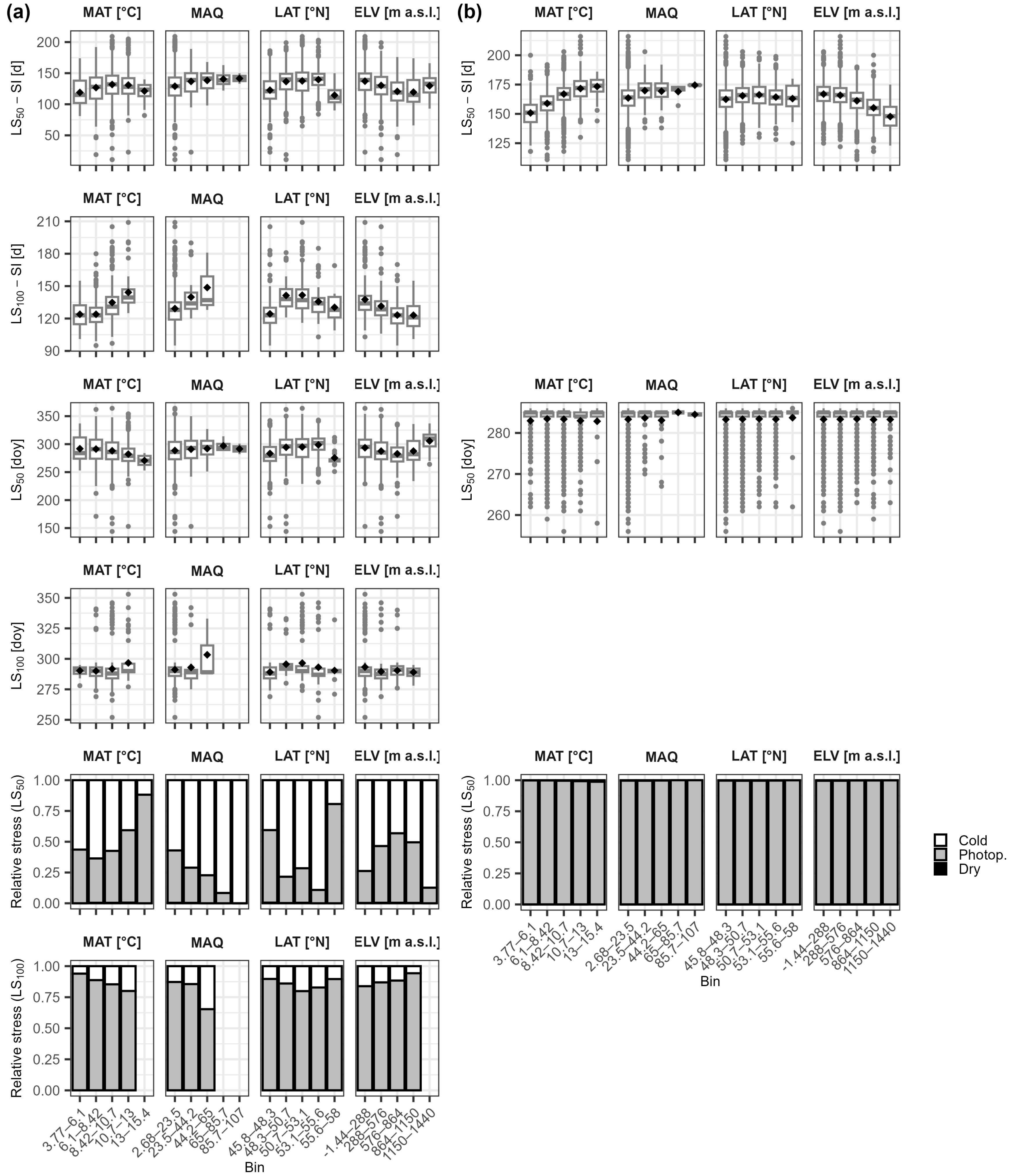

Figure S3. Date and duration of senescence. Panel (a) and (b) are based on predictions by the DP3 model calibrated with the LS_{50}-LS_{100} versus LS_{50} samples, respectively (Sect. 2.4). The top row of each panel illustrates the duration of senescence according to LS_{50} (i.e., the difference in days [d] of the day when 50% of the leaves having turned color or having fallen, LS_{50}, minus the day of senescence induction, SI). The second row of panel (a) shows the duration of senescence according to LS_{100} (i.e., the difference in days [d] of the day when 100% of the leaves having turned color or having fallen, LS_{100}, minus SI). The third row of panel (a) and the middle row of panel (b) visualize the day of year [doy] of LS_{50}, while the fourth row of panel (a) do so for LS_{100}. The fifth row of panel (a) and the bottom row of panel (b) illustrate the relative amount of cold stress, photoperiod stress, and dry stress that accumulated between SI and LS_{50}. Accordingly, the bottom row of panel (a) shows these relative amounts for the period from SI to LS_{100}. In every row, the x-axis is divided in equally distributed bins among mean annual temperature (MAT, °C), mean annual Keetch and Byram drought index (MAQ), latitude (LAT, °N), and elevation (ELV; m a.s.l.). While the mean and median dates are marked with black dots and grey lines, respectively, the most extreme values are indicated with dots if outside ±1.5 times the inner quartile range from the 1st and 3rd quartile, and with whiskers otherwise.

S3.2 Model error

Table S9. Linear mixed-effects model (LMM) explaining the model error

Coefficient	Value	SE	*t* statistic	*p*-value	$\underline{BF}_{01}$	Lower 0.5%	Upper 99.5%
Intercept	8.1104	1.5297	5.3021	**0.0000**	**0.0000**	4.1700	12.0507
CDD [d]	–1.8144	0.2367	–7.6656	**0.0000**	**0.0000**	–2.4241	–1.2047
DM2 [d]	–0.7348	0.2367	–3.1043	**0.0019**	0.0414	–1.3445	–0.1251
PIA [d]	–0.6290	0.2509	–2.5069	0.0122	0.1785	–1.2754	0.0173
$DP3_{LS_{50}}$ [d]	0.1038	0.2367	0.4385	0.6610	1.0000	–0.5059	0.7135
δMAT [d °C^{-1}]	–2.0028	0.1306	–15.3347	**0.0000**	**0.0000**	–2.3393	–1.6664
δMAQ [d]	0.0901	0.0179	5.0172	**0.0000**	**0.0000**	0.0438	0.1363
δA_{net} [d mol C^{-1} m^{-2}]	0.4148	0.0160	25.9480	**0.0000**	**0.0000**	0.3736	0.4560
δLAT [d °$^{-1}$]	2.1126	0.4724	4.4725	**0.0000**	**0.0003**	0.8959	3.3294
δELV [d m^{-1}]	0.0113	0.0031	3.6690	**0.0002**	*0.0072*	0.0034	0.0193
SUI [d]	–6.1036	1.8142	–3.3643	**0.0008**	0.0193	–10.7770	–1.4302
GER [d]	–7.8265	2.2319	–3.5067	**0.0005**	0.0124	–13.5758	–2.0772
GBR [d]	–24.6277	2.9215	–8.4297	**0.0000**	**0.0000**	–32.1534	–17.1020
CDD × δMAT [d °C^{-1}]	–0.1457	0.1887	–0.7720	0.4401	1.0000	–0.6318	0.3404
DM2 × δMAT [d °C^{-1}]	–0.1771	0.1887	–0.9386	0.3480	1.0000	–0.6632	0.3090
PIA × δMAT [d °C^{-1}]	0.0961	0.1888	0.5092	0.6106	1.0000	–0.3901	0.5824
$DP3_{LS_{50}}$ × δMAT [d °C^{-1}]	–0.0431	0.1887	–0.2283	0.8194	1.0000	–0.5292	0.4430
CDD × δMAQ [d]	–0.0537	0.0276	–1.9495	0.0512	0.4806	–0.1247	0.0173
DM2 × δMAQ [d]	–0.0502	0.0276	–1.8225	0.0684	0.5709	–0.1212	0.0208
PIA × δMAQ [d]	–0.0474	0.0281	–1.6869	0.0916	0.6704	–0.1197	0.0250
$DP3_{LS_{50}}$ × δMAQ [d]	–0.0147	0.0276	–0.5332	0.5939	1.0000	–0.0857	0.0563
CDD × δA_{net} [d mol C^{-1} m^{-2}]	0.0173	0.0236	0.7323	0.4640	1.0000	–0.0435	0.0781
DM2 × δA_{net} [d mol C^{-1} m^{-2}]	0.0093	0.0236	0.3958	0.6922	1.0000	–0.0515	0.0702
PIA × δA_{net} [d mol C^{-1} m^{-2}]	0.0466	0.0236	1.9739	0.0484	0.4639	–0.0142	0.1074
$DP3_{LS_{50}}$ × δA_{net} [d mol C^{-1} m^{-2}]	–0.0031	0.0236	–0.1327	0.8945	1.0000	–0.0639	0.0577
CDD × δLAT [d °$^{-1}$]	–0.0573	0.1376	–0.4162	0.6773	1.0000	–0.4117	0.2972
DM2 × δLAT [d °$^{-1}$]	–0.0665	0.1376	–0.4830	0.6291	1.0000	–0.4209	0.2880
PIA × δLAT [d °$^{-1}$]	–0.0344	0.1378	–0.2495	0.8030	1.0000	–0.3892	0.3205
$DP3_{LS_{50}}$ × δLAT [d °$^{-1}$]	0.0172	0.1376	0.1252	0.9004	1.0000	–0.3372	0.3716
CDD × δELV [d m^{-1}]	–0.0012	0.0013	–0.9438	0.3453	1.0000	–0.0045	0.0021
DM2 × δELV [d m^{-1}]	–0.0011	0.0013	–0.8856	0.3759	1.0000	–0.0044	0.0021
PIA × δELV [d m^{-1}]	–0.0014	0.0013	–1.0789	0.2806	0.9940	–0.0046	0.0019
$DP3_{LS_{50}}$ × δELV [d m^{-1}]	0.0000	0.0013	0.0139	0.9889	1.0000	–0.0032	0.0033

Note: The LMM was fitted to the response variable 'model error' [i.e., $x_{s,i} - x_{o,i}$, the difference in days calculated as the predicted minus the observed date for each stage and site-year (*i*)] in the validation sample (Sect. 2.6 and S2.3), based on 41 068 observations, and resulted in an adjusted R^2 of 0.44 and a proportion of the deviance explained of 0.44. The random intercepts were grouped by site with σ_b = 9.32 d (99% confidence interval 8.26 ≤ σ_b ≤ 10.52 d). SE is the standard error, while 'Lower 0.05%' and 'Upper 99.5%' indicate the lower and upper boundaries of the 99% confidence interval. Bold *p*-values are indicate significant fixed effects at α = 0.01 (i.e., $p \leq 0.005$ for a two-sided hypothesis test), bold and italic minimum Bayes factors ($\underline{BF}_{01}$) indicate decisive and very strong fixed effects (i.e., $\underline{BF}_{01} \leq 1/1000$ and $\underline{BF}_{01} \leq 1/100$, respectively). The intercept represents the base line, i.e., the model error according to the Null model for the reference level Austria. CDD, DM2, PIA, and DP3 are the factorized models, while SUI, GER, and GBR are the factorized countries Switzerland, Germany, and Great Britain, respectively. The random intercepts were grouped by 'site'. All models ware calibrated and validated with the LS_{50} sample (Sect. 2.4).

Table S10. Interacting effects according to the LMM

Variable	Model	Country	Estimate	SE	0.5 %	99.5 %	Equation
Country [d]	Null	AUT	8.11	1.53	4.17	12.05	β_0
		SUI	2.01	1.50	–1.86	5.87	β_0 + SUI
		GER	0.28	1.34	–3.16	3.73	β_0 + GER
		GBR	–16.52	2.02	–21.71	–11.32	β_0 + GBR
	CDD	AUT	6.30	1.55	2.31	10.28	β_0 + CDD
		SUI	0.19	1.52	–3.72	4.11	β_0 + CDD + SUI
		GER	–1.53	1.33	–4.96	1.90	β_0 + CDD + GER
		GBR	–18.33	2.00	–23.49	–13.17	β_0 + CDD + GBR
	DM2	AUT	7.38	1.55	3.39	11.36	β_0 + DM2
		SUI	1.27	1.52	–2.64	5.18	β_0 + DM2 + SUI
		GER	–0.45	1.33	–3.88	2.98	β_0 + DM2 + GER
		GBR	–17.25	2.00	–22.41	–12.09	β_0 + DM2 + GBR
	PIA	AUT	7.48	1.52	3.56	11.41	β_0 + PIA
		SUI	1.38	1.49	–2.47	5.23	β_0 + PIA + SUI
		GER	–0.35	1.36	–3.84	3.15	β_0 + PIA + GER
		GBR	–17.15	2.04	–22.40	–11.89	β_0 + PIA + GBR
	$DP3_{LS_{50}}$	AUT	8.21	1.55	4.23	12.20	β_0 + $DP3_{LS_{50}}$
		SUI	2.11	1.52	–1.80	6.02	β_0 + $DP3_{LS_{50}}$ + SUI
		GER	0.39	1.33	–3.05	3.82	β_0 + $DP3_{LS_{50}}$ + GER
		GBR	–16.41	2.00	–21.57	–11.25	β_0 + $DP3_{LS_{50}}$ + GBR
δELV [d 100 m^{-1}]	Null	AC	1.13	0.31	0.34	1.93	100 δELV
	CDD		1.01	0.32	0.20	1.83	100 (δELV + CDD × δELV)
	DM2		1.02	0.32	0.20	1.84	100 (δELV + DM2 × δELV)
	PIA		1.00	0.32	0.18	1.82	100 (δELV + PIA × δELV)
	$DP3_{LS_{50}}$		1.14	0.32	0.32	1.95	100 (δELV + $DP3_{LS_{50}}$ × δELV)
δLAT [d $°N^{-1}$]	Null		2.11	0.47	0.90	3.33	δLAT
	CDD		2.06	0.48	0.82	3.29	δLAT + CDD × δLAT
	DM2		2.05	0.48	0.81	3.28	δLAT + DM2 × δLAT
	PIA		2.08	0.48	0.84	3.31	δLAT + PIA × δLAT
	$DP3_{LS_{50}}$		2.13	0.48	0.90	3.36	δLAT + $DP3_{LS_{50}}$ × δLAT
δMAQ [d 100^{-1}]	Null		9.01	1.79	4.38	13.63	100 δMAQ
	CDD		3.63	2.29	–2.28	9.54	100 (δMAQ + CDD × δMAQ)
	DM2		3.98	2.29	–1.93	9.89	100 (δMAQ + DM2 × δMAQ)
	PIA		4.27	2.37	–1.83	10.37	100 (δMAQ + PIA × δMAQ)
	$DP3_{LS_{50}}$		7.54	2.29	1.63	13.45	100 (δMAQ + $DP3_{LS_{50}}$ × δMAQ)
δMAT [d 10$°C^{-1}$]	Null		–20.03	1.31	–23.39	–16.66	10 δMAT
	CDD		–21.49	1.69	–25.84	–17.13	10 (δMAT + CDD × δMAT)
	DM2		–21.80	1.69	–26.16	–17.44	10 (δMAT + DM2 × δMAT)
	PIA		–19.07	1.69	–23.43	–14.71	10 (δMAT + PIA × δMAT)
	$DP3_{LS_{50}}$		–20.46	1.69	–24.82	–16.10	10 (δMAT + $DP3_{LS_{50}}$ × δMAT)
δA_{net} [d 10 mol C^{-1} m^{-2}]	Null		4.15	0.16	3.74	4.56	10 δA_{net}
	CDD		4.32	0.21	3.78	4.86	10 (δA_{net} + CDD × δA_{net})
	DM2		4.24	0.21	3.70	4.78	10 (δA_{net} + DM2 × δA_{net})
	PIA		4.61	0.21	4.08	5.15	10 (δA_{net} + PIA × δA_{net})
	$DP3_{LS_{50}}$		4.12	0.21	3.58	4.65	10 (δA_{net} + $DP3_{LS_{50}}$ × δA_{net})

Note: The interacting effects of the LMM (Table S9) were calculated with the Delta method (Chpt. 5.1.4 in Fox and Weisberg, 2019; Chpt. 9.9 in Wasserman, 2004) according to the displayed equation, together with their standard error (SE) and 99% confidence interval (i.e., the 0.5% lower bound and 99.5% upper bound). AUT, SUI, GER, and GBR refer to the countries Austria, Switzerland, Germany, and Great Britain, respectively, while AC marks estimates across countries. The unit for δA_{net} is d 10 mol C^{-1} m^{-2}.

Table S11. Impact on the variance in the model error explained by the LMM

Explanatory variable	**Impact**	**Accumulated**	***p*-value**	**$\underline{BF}_{01}$**
Site	0.9164	0.9164	**0.0000**	**0.0000**
δA_{net}	0.0591	0.9755	**0.0000**	**0.0000**
δMAT	0.0195	0.9950	**0.0000**	**0.0000**
Model	0.0032	0.9982	**0.0000**	**0.0000**
δMAQ	0.0011	0.9993	**0.0000**	**0.0000**
Model × δMAQ	0.0003	0.9996	0.1799	0.8997
Model × δA_{net}	0.0002	0.9998	0.3213	1.0000
Model × δMAT	0.0001	0.9999	0.7026	1.0000
Model × δELV	0.0001	1.0000	0.7110	1.0000
δLAT	0.0000	1.0000	**0.0000**	**0.0000**
δELV	0.0000	1.0000	**0.0000**	**0.0000**
Country	0.0000	1.0000	**0.0000**	**0.0000**
Model × δLAT	0.0000	1.0000	0.9770	1.0000

Note: The type-III analysis of variance (ANOVA; Sect. 2.6 and S2.3) was based on the LMM (Table S9) and thus on 54 834 observations. For each explanatory variable (i.e., fixed and random effects), the impact on the variance in the model error as explained by the LMM is given, together with the accumulated impact when ordered by impact. Bold *p*-values are significant at $\alpha = 0.01$ (i.e., $p \leq 0.01$ for a one-sided hypothesis test) and bold minimum Bayes factors ($\underline{BF}_{01}$) are decisive (i.e., $\underline{BF}_{01} \leq 1/1000$).

References

Akaike, H.: A new look at the statistical model identification, IEEE Trans. Autom. Control, 19, 716–723, https://doi.org/10.1109/TAC.1974.1100705, 1974.

Baayen, R. H., Davidson, D. J., and Bates, D. M.: Mixed-effects modeling with crossed random effects for subjects and items, J. Mem. Lang., 59, 390–412, https://doi.org/10.1016/j.jml.2007.12.005, 2008.

Brock, T. D.: Calculating solar radiation for ecological studies, Ecol. Model., 14, 1–19, https://doi.org/10.1016/0304-3800(81)90011-9, 1981.

Burnham, K. P. and Anderson, D. R.: Multimodel Inference: Understanding AIC and BIC in Model Selection, Sociol. Methods Res., 33, 261–304, https://doi.org/10.1177/0049124104268644, 2004.

Candelieri, A.: A gentle introduction to Bayesian Optimization, 2021 Winter Simulation Conference (WSC), Phoenix, AZ, and virtual, 1–16, https://doi.org/10.1109/WSC52266.2021.9715413, 2021.

Collatz, G. J., Ball, J. T., Grivet, C., and Berry, J. A.: Physiological and environmental-regulation of stomatal conductance, photosynthesis and transpiration - A model that includes laminar boundary-layer, Agric. For. Meteorol., 54, 107–136, https://doi.org/10.1016/0168-1923(91)90002-8, 1991.

Farquhar, G. D., von Caemmerer, S., and Berry, J. A.: A biochemical model of photosynthetic CO2 assimilation in leaves of C3 species, Planta, 149, 78–90, https://doi.org/10.1007/bf00386231, 1980.

Fisher, R. A. and Russell, E. J.: On the mathematical foundations of theoretical statistics, Philos. Trans. R. Soc. Lond. Ser. Contain. Pap. Math. Phys. Character, 222, 309–368, https://doi.org/10.1098/rsta.1922.0009, 1997.

Foster, G. R., McCool, D. K., Renard, K. G., and Moldenhauer, W. C.: Conversion of the universal soil loss equation to SI metric units, J. Soil Water Conserv., 36, 355–359, 1981.

Fox, J. and Weisberg, S.: An R Companion to Applied Regression, Third., SAGE, Los Angeles, 2019.

Geodesy: Approximate formulas for the transformation between Swiss projection coordinates and WGS84, 2016.

Gerten, D., Schaphoff, S., Haberlandt, U., Lucht, W., and Sitch, S.: Terrestrial vegetation and water balance - hydrological evaluation of a dynamic global vegetation model, J. Hydrol., 286, 249–270, https://doi.org/10.1016/j.jhydrol.2003.09.029, 2004.

Gupta, H. V., Kling, H., Yilmaz, K. K., and Martinez, G. F.: Decomposition of the mean squared error and NSE performance criteria: Implications for improving hydrological modelling, J. Hydrol., 377, 80–91, https://doi.org/10.1016/j.jhydrol.2009.08.003, 2009.

Haxeltine, A. and Prentice, I. C.: BIOME3: An equilibrium terrestrial biosphere model based on ecophysiological constraints, resource availability, and competition among plant functional types, Glob. Biogeochem. Cycles, 10, 693–709, https://doi.org/10.1029/96gb02344, 1996.

Haxeltine, A., Prentice, I. C., and Creswell, D. I.: A coupled carbon and water flux model to predict vegetation structure, J. Veg. Sci., 7, 651–666, https://doi.org/10.2307/3236377, 1996.

Keetch, J. J. and Byram, G. M.: A Drought Index for Forest Fire Control, Department of Agriculture, Forest Service, Southeastern Forest Experiment Station, Asheville, NC: U.S., 1968.

Kling, H., Fuchs, M., and Paulin, M.: Runoff conditions in the upper Danube basin under an ensemble of climate change scenarios, J. Hydrol., 424–425, 264–277, https://doi.org/10.1016/j.jhydrol.2012.01.011, 2012.

Kloos, S., Klosterhalfen, A., Knohl, A., and Menzel, A.: Decoding autumn phenology: Unraveling the link between observation methods and detected environmental cues, Glob. Change Biol., 30, e17231, https://doi.org/10.1111/gcb.17231, 2024.

Lu, X. and Keenan, T. F.: No evidence for a negative effect of growing season photosynthesis on leaf senescence timing, Glob. Change Biol., 28, 3083–3093, https://doi.org/10.1111/gcb.16104, 2022.

Maes, F., Wehenkel, L., and Ernst, D.: Meta-learning of exploration/exploitation strategies: The Multi-armed bandit case, Agents and Artificial Intelligence, 100–115, 2013.

Meier, M. and Bigler, C.: Process-oriented models of autumn leaf phenology: ways to sound calibration and implications of uncertain projections, Geosci. Model Dev., 16, 7171–7201, https://doi.org/10.5194/gmd-16-7171-2023, 2023.

Swiss phenology network: https://www.meteoswiss.admin.ch/weather/measurement-systems/land-based-stations/swiss-phenology-network.html, last access: 29 January 2025.

Pinheiro, J. C. and Bates, D. M.: Mixed-effects models in S and S-PLUS, Springer, New York, 528 S. pp., 2000.

R Core Team: R: A language and environment for statistical computing, 2025.

Shaw, H. G.: Centigrade-Fahrenheit temperature conversion, J. Chem. Educ., 8, 727, 1931.

Sitch, S., Prentice, I. C., Smith, B., Cramer, W., Kaplan, J. O., Lucht, W., Sykes, M. T., Thonicke, K., and Venevsky, S.: LPJ - A Coupled Model Of Vegetation Dynamics And The Terrestrial Carbon Cycle. https://www.researchgate.net/publication/37456884, 2000.

Wang, H., Gao, C., and Ge, Q.: Low temperature and short daylength interact to affect the leaf senescence of two temperate tree species, Tree Physiol., 42, 2252–2265, https://doi.org/10.1093/treephys/tpac068, 2022.

Wasserman, L.: All of Statistics. A Concise Course in Statistical Inference, 1st ed., Springer New York, NY, 2004.

Wohlfahrt, G. and Gu, L.: The many meanings of gross photosynthesis and their implication for photosynthesis research from leaf to globe, Plant Cell Environ., 38, 2500–2507, https://doi.org/10.1111/pce.12569, 2015.

Wood, S. N.: Fast stable restricted maximum likelihood and marginal likelihood estimation of semiparametric generalized linear models, J. R. Stat. Soc. Ser. B Stat. Methodol., 73, 3–36, https://doi.org/10.1111/j.1467-9868.2010.00749.x, 2011.

Wood, S. N.: Generalized additive models: An introduction with R, 2nd edition., Chapman and Hall/CRC, New York, 2017.

Woods, H. W.: Centigrade-fahrenheit temperature conversion, J. Chem. Educ., 8, 370, 1931.

Xiang, Y., Sun, D. Y., Fan, W., and Gong, X. G.: Generalized Simulated Annealing algorithm and its application to the Thomson model, Phys. Lett. A, 233, 216–220, https://doi.org/10.1016/s0375-9601(97)00474-x, 1997.

Xiang, Y., Gubian, S., and Martin, F.: Generalized Simulated Annealing, in: Computational Optimization in Engineering - Paradigms and Applications, 25–46, 2017.

Yates, F.: The analysis of multiple classifications with unequal numbers in the different classes, J. Am. Stat. Assoc., 29, 51–66, https://doi.org/10.2307/2278459, 1934.

Zani, D., Crowther, T. W., Mo, L., Renner, S. S., and Zohner, C. M.: Increased growing-season productivity drives earlier autumn leaf senescence in temperate trees, Science, 370, 1066–1071, https://doi.org/10.1126/science.abd8911, 2020.